

MSTT-199: MRI Dataset for Musculoskeletal Soft Tissue Tumor Segmentation

Tahsin Reasat^a, Stephen Chenard^b, Akhil Rekulapelli^b, Nicholas Chadwick^c, Joanna Shechtel^c, Katherine van Schaik^c, David S. Smith^{a,c,d}, and Joshua Lawrenz^b

^aDepartment of Electrical and Computer Engineering, Vanderbilt University, Nashville, 37235, Tennessee, USA

^bDepartment of Orthopædic Surgery, Vanderbilt University Medical Center, Nashville, 37232, Tennessee, USA

^cDepartment of Radiology and Radiological Sciences, Vanderbilt University Medical Center, Nashville, 37232, Tennessee, USA

^dInstitute of Imaging Science, Vanderbilt University Medical Center, Nashville, 37232, Tennessee, USA

ABSTRACT

Accurate musculoskeletal soft tissue tumor segmentation is vital for assessing tumor size, location, diagnosis, and response to treatment, thereby influencing patient outcomes. However, segmentation of these tumors requires clinical expertise, and an automated segmentation model would save valuable time for both clinician and patient. Training an automatic model requires a large dataset of annotated images. In this work, we describe the collection of an MR imaging dataset of 199 musculoskeletal soft tissue tumors from 199 patients. We trained segmentation models on this dataset and then benchmarked them on a publicly available dataset. Our model achieved the state-of-the-art dice score of 0.79 out of the box without any fine tuning, which shows the diversity and utility of our curated dataset. We analyzed the model predictions and found that its performance suffered on fibrous and vascular tumors due to their diverse anatomical location, size, and intensity heterogeneity. The code and models are available in the following github repository [[github](#)].

1 Introduction

A musculoskeletal soft tissue tumor (MSTT) is an abnormal growth or mass that develops within the soft tissues of the body that support and connect the musculoskeletal system¹. Soft tissues encompass a variety of structures, including muscles, tendons, ligaments, fat, blood vessels, nerves, and connective tissues. MSTTs can arise from any of these tissues and can be either benign (non-cancerous) or malignant (cancerous). Benign MSTTs, such as lipomas or fibromas, typically grow slowly and do not invade surrounding tissues or metastasize to other parts of the body. Malignant MSTTs, on the other hand, can be aggressive and have the potential to spread to nearby organs or distant sites, posing a more significant health risk.¹

Tumor segmentation allows for precise delineation of the tumor boundaries, providing accurate measurements of size and shape. This information is essential for disease staging and determining the appropriate treatment strategy². Moreover, precise segmentation facilitates the monitoring of tumor progression and response to therapy over time, enabling clinicians to make timely adjustments to the treatment plan². Additionally, segmentation enables the identification of heterogeneous regions within the tumor allowing diagnosis of varying levels of malignancy².

A crucial step of building an automated model that identifies benign and malignant tumors is the manual segmentation of the tumor³⁻⁶. Segmentation is challenging, as tumor appearance can vary in shape, intensity, and tissue composition². Additionally, the presence of artifacts such as noise, motion,

and magnetic susceptibility can further obscure tumor boundaries, making segmentation challenging. Moreover, the lack of standardized protocols for acquiring MRI data, leading to variations in image contrast and quality across different institutions and scanners adds to the difficulty. Even if the clinician has sufficient expertise, manual delineation of tumors in three dimensions is a time-consuming process, taking up to half an hour per MRI volume⁷.

In recent times, researchers have strived to automate the MSTT segmentation process by employing various classical machine learning⁸ and deep learning^{9–11} based methods. Researchers have explored models that take both single and multimodal images (MRI, PET, CT scans) as input and predict tumor segmentation. These models have been trained and evaluated using a small dataset of 51 patients presented in¹². The progress of automatic MSTT segmentation models has lagged due to the unavailability of large diversified datasets. To address this problem we have curated a dataset and trained a segmentation model using the data. The contributions of this paper are fourfold:

- We created an MSTT segmentation dataset with 199 patients and plan to make it publicly available for future research;
- We described our process of selecting the patients, setting up the labeling platform, the annotation protocol, and the curation method;
- We created a segmentation model based on the curated data which achieves state-of-the-art (SOTA) result on the only available public dataset and analyzed the results; and
- We identify easy versus hard-to-detect types of tumor and make suggestions for future model development as well as data collection.

The paper is organized in the following sections. Section 2 contains the detailed creation of the dataset. Section 3 includes the architectural explanation of the segmentation models used in this work. Section 4 contains the experimental setup and result analysis. And finally the paper is concluded in Section 5.

2 MSTT-199: Dataset Description

In this section, we describe the process of patient selection, data annotation, annotation protocol, and data curation method.

2.1 Patient Selection

After receiving institutional review board approval, we queried our institution's orthopaedic oncology registry, which includes all patients treated for an MSTT at our institution since 1987. Using this registry, we initially identified 2,639 patients who underwent definitive oncological resection at Vanderbilt University Medical Center and had one of the following diagnoses on final pathological review: schwannoma (benign nerve tumor), MPNST (malignant peripheral nerve sheath tumor), well-differentiated liposarcoma (benign fat tumor), dedifferentiated liposarcoma (malignant fat tumor), desmoid fibromatosis (benign fibrous tumor), undifferentiated pleomorphic sarcoma (malignant fibrous tumor), hemangioma or arteriovenous malformation (benign vascular tumor), angiosarcoma (malignant vascular tumor), myxoma (benign myxoid tumor), or myxoid fibrosarcoma (malignant myxoid tumor). The tissue type of the tumors were divided in five broad categories Fibrous, Fat, Myxoid, Nerve, and Vascular.

We retrospectively reviewed the electronic health records of patients in reverse chronological order and sequentially included patients who had a tumor with largest dimension greater than 3 cm, and a pre-operative MRI that included both an axial T1 and an axial T2 fat-saturation sequence. Patients with MRI

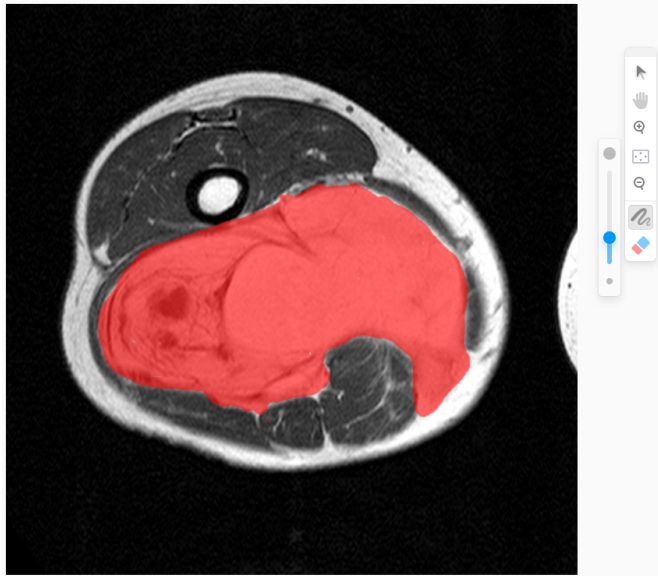


Figure 1. The Label Studio annotation setup used for this project. The annotators can choose a brush size and annotate the tumor at different granularity.

sequences that were deemed to be incomplete or of poor image quality as determined by a board-certified orthopedic oncologist or musculoskeletal radiologist were excluded. Records were reviewed until ~40 eligible patients with each tumor tissue type (Fibrous, Fat, Myxoid, Nerve, Vascular) were included, or all available records were exhausted. This resulted in a collection of 199 patients with 199 MSTTs.

2.2 Labeling Platform

We selected LabelStudio¹³ as our data annotation platform. LabelStudio provides a web browser-based labeling platform that has minimal user setup overhead at the annotator's end. Radiologists can log in through the provided URL, create an account, and start annotating the assigned image. LabelStudio provides a customizable user management system through which user activity and dataset progress can be tracked with ease.

Both T1- and T2-weighted images were present for each tumor and registered using ANTs¹⁴ algorithm on the 3D Slicer software¹⁵. The smaller image of the pair was also resampled to match the resolution of the largest image. Following registration, the axial slices of MRI images were exported to PNG files and listed on the project along with necessary metadata such as patient ID, modality, type of tumor, slice instance number, anatomy, etc. While logged in to the platform, the annotator could search images via patient ID and modality and sort by instance number. After selecting an image, the annotator drew segmentation masks on top of the tumor area using a brush tool. A screenshot of the annotation user interface is shown in Fig. 1. The size of the brush tool can be varied for fine or coarse masks. The choice of brush size creates a trade-off between accuracy and annotation time.

2.3 Annotation Protocol

Annotations were done primarily on the T2-weighted images except for the Fat tumors which were mostly done on the T1-weighted images due to better tumor visibility. The axial slices of the images were uploaded on a privately deployed annotation platform called LabelStudio¹⁶. The annotators logged into the platform to annotate and submit their annotations.

The data was annotated in three stages. In the first stage, a radiologist (K) annotated the center slice of

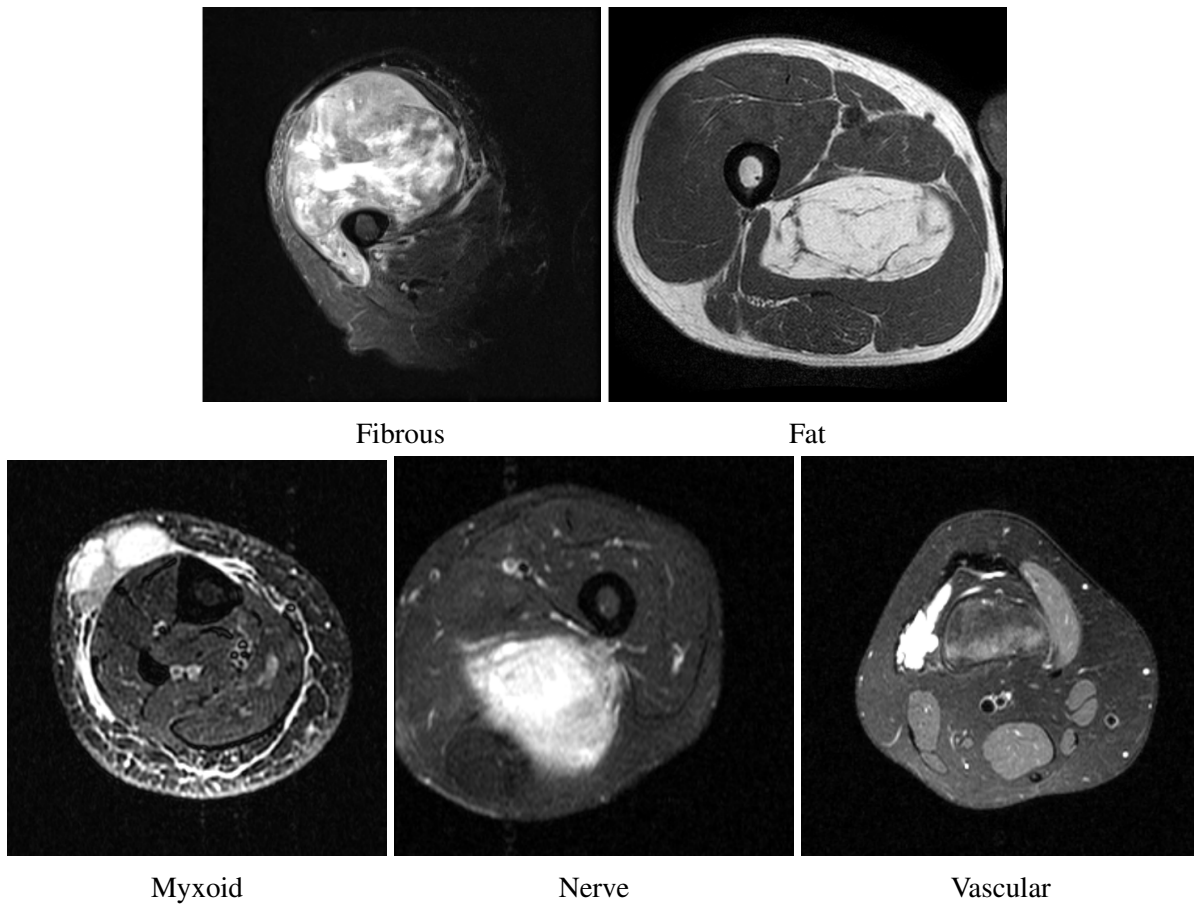


Figure 2. Example of different tissue types present in the MSTT-199 corpus. The Fat tumor is brighter on T1 while the rest of the tissue types are brighter on T2.

the tumor present in each MRI. In the second stage, three annotators (S, A, T) annotated the adjacent slices of the annotation following the guiding annotations done by K. The questions or confusion that arose during the second stage were all mitigated via discussion with the radiologist.

In the final stage, the complete annotations were sent to the radiologists, J, K, and N for final review. The patients were randomly divided among the three radiologists and had one radiologist review per image.

The radiologists identified tumor area regions by looking at T2 signal hyperintensity or edema on fluid-sensitive sequences and also using the contrast between normal muscle or tumors and surrounding fat planes on the conventional T1 sequences. While annotating most of the central mass is demarcated; however, some tumors may have narrow tail-like extension from the margins of the mass which might be excluded. Radiologists took image noise and artifact into consideration during the interpretation of the MR images and discounted them without difficulty.

2.4 Dataset Statistics

The tissue type statistics and anatomy distribution in the dataset are shown in Table 1, and examples of tissue images are shown in Fig. 2. Although we assembled a balanced dataset for each tissue type, it was difficult to keep the anatomical location distribution balanced. MSTTs are most prevalent in the extremities with very few occurrences in the trunk or head and neck region^{2,17}. Fig. 3 shows the tumor size variation

Tumor Site	Tissue Type					Total
	Fibrous	Fat	Myxoid	Nerve	Vascular	
thigh	21	35	26	10	11	103
leg	5	2	2	11	5	25
glute	0	2	11	3	3	19
forearm	1	0	0	4	8	13
arm	1	1	0	8	0	10
shoulder	3	0	0	0	4	7
pelvis	1	0	0	1	2	4
hand	0	0	0	1	3	4
foot	1	0	0	1	1	3
chest wall	2	0	1	0	0	3
neck	2	0	0	0	1	3
abdominal wall	2	0	0	0	0	2
axilla	0	0	0	1	0	1
back	1	0	0	0	0	1
flank	0	0	0	0	1	1
Total	40	40	40	40	39	199

Table 1. Tissue type and anatomical distribution of the tumors.

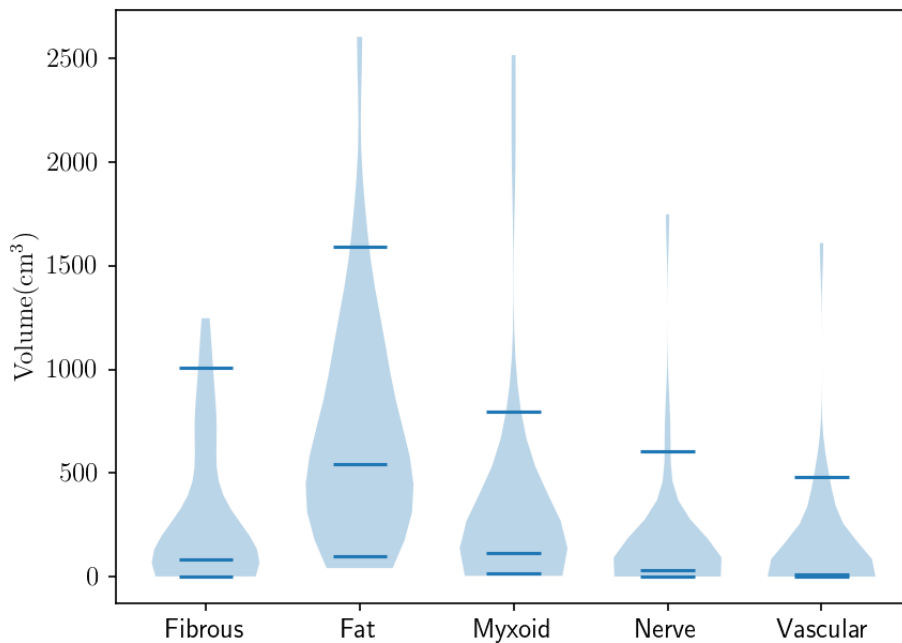


Figure 3. Tumor volume distribution. Fat tumors were on average larger than those for the other subtypes, while the other four subtypes were more similar.

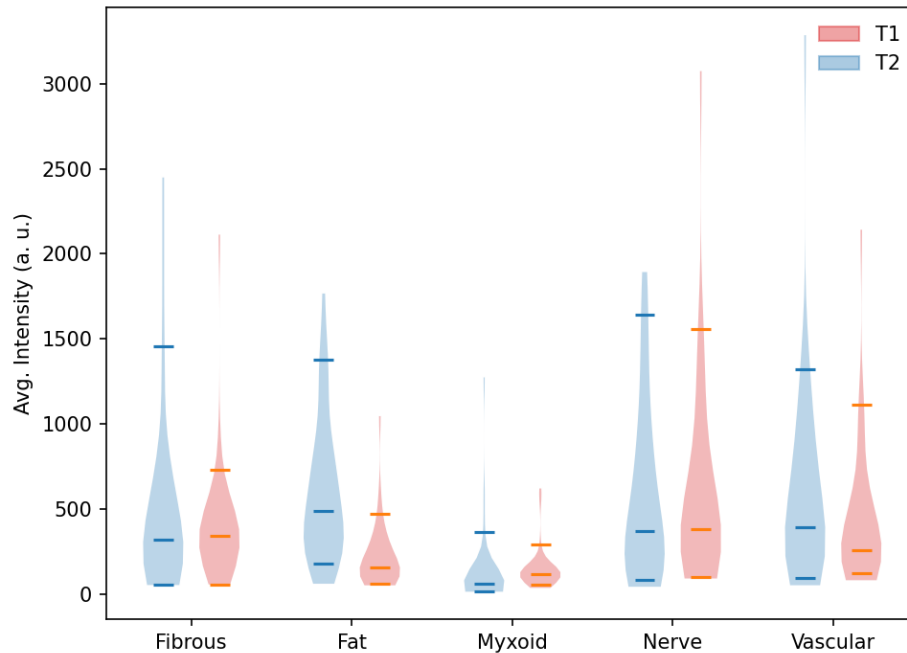


Figure 4. Average tumor intensity distribution in T1 and T2 image. Myxoid tumors tended to have a lower intensity on average on both T1 and T2, while the other tumors were more similar in intensity.

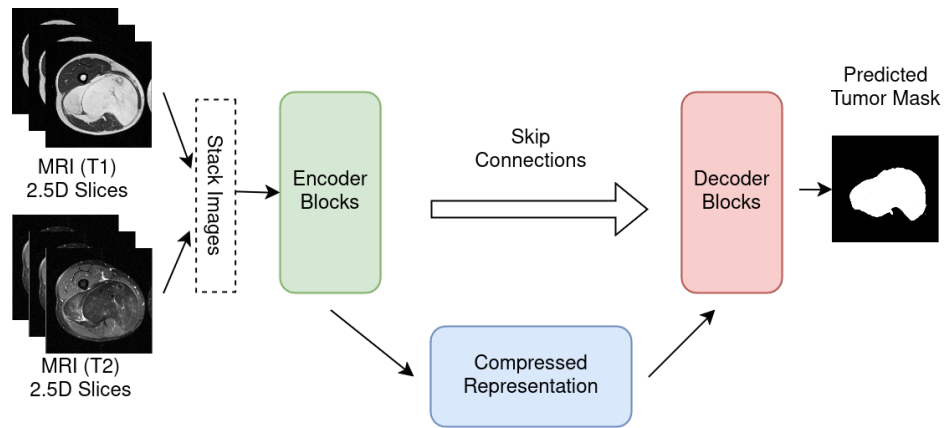
for different tissue types. The Fat tumors are usually larger in size, and the nerve and vascular tumors are comparatively smaller. Fig. 4 shows the intensity distribution across the tissue types. For fibrous, nerve, and vascular tissue types there is an overlap in the distribution of the intensities from the two modalities. However, Fat tumors show higher intensity on T1 (Fig. 2), whereas, the myxoid tumors show a higher intensity distribution on T2. This justifies our choice to annotate the fat tumors on T1 modality and the myxoid tumors on T2 modality.

3 Segmentation Models

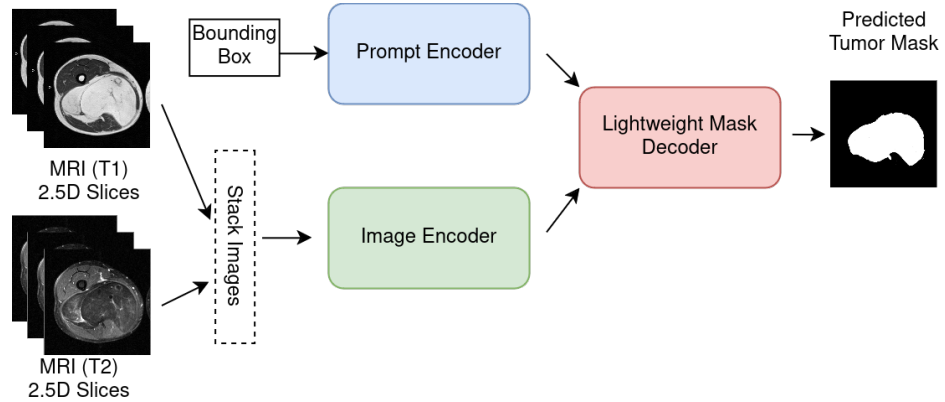
In this section, we describe the segmentation model architectures and the loss function used to train the model.

3.1 Architecture

We used the U-Net¹⁸ architecture as our segmentation model. The U-Net segmentation model is a convolutional neural network architecture initially designed for biomedical image segmentation tasks¹⁸. U-Net has two main components: an encoder and a decoder. The encoder downsamples the input image in steps and reduces it to a representation rich in information but with the loss of spatial resolution. The decoder takes this representation and gradually upsamples it to reconstruct a probability output having the spatial size of the image. The output map is thresholded to create a binary mask of the foreground object. There are shortcut connections (or skip connections) between different stages of the encoder and decoder that have similar feature dimensions which enables information flow between feature blocks. The encoder, decoder, and shortcut connections create a U-shaped visualization for the model (Fig. 5a), hence the name U-Net.



(a) U-Net



(b) Segment Anything Model (SAM)

Figure 5. The segmentation model architectures. The input to both the segmentation models is a multi-modal MRI image (T1 and T2). The 2.5-D slices coming from each modality are stacked to create a six-channel input. **5a)** The U-Net segmentation model has a U-shaped structure due to skip connections going from the encoders to the decoders. **5b)** The SAM model has an additional prompt encoder. For automatic segmentation, the prompt encoder receives a bounding box drawn over the full image.

3.1.1 Encoder

The encoder consists of a series of convolutional blocks. Each block typically consists of two consecutive convolutional layers followed by a rectified linear unit (ReLU)¹⁹ activation function and a max-pooling layer. The purpose of this path is to capture context and spatial information from the input image while reducing its spatial dimensions. As the network progresses through the contracting path, the receptive field increases while the spatial resolution decreases.

3.1.2 Decoder

The decoder is responsible for upsampling the feature maps to the original input resolution. Each block in this path consists of an upsampling operation (usually transposed convolution or interpolation), followed by concatenation with feature maps from the encoder path, and then a series of convolutional layers. The concatenation operation helps in preserving fine-grained details from the encoder path, facilitating precise segmentation.

3.1.3 Shortcut Connections

One of the key features of U-Net is the skip connections that directly connect corresponding layers between the encoder and the decoder. These connections allow the network to bypass the loss of spatial information during downsampling and aid in the precise localization of objects in the segmentation masks. Skip connections provide a shortcut for gradient flow during training, helping to mitigate the vanishing gradient problem and enabling faster convergence.

3.1.4 Final Layer

The final layer of the network consists of a 1×1 convolutional layer followed by a sigmoid activation function. This layer produces the segmentation mask with the same spatial dimensions as the input image, where each pixel represents the predicted class or label.

3.2 Segment Anything Model (SAM)

The segment anything model (SAM)²⁰ is a foundational model proposed for image segmentation. It has been trained on a large dataset of diverse images and can be applied to a wider range of segmentation tasks. This model has been further fine tuned on a large-scale medical image segmentation dataset with 1,570,263 medical image-mask pairs, covering 10 imaging modalities, over 30 cancer types, and a multitude of imaging protocols to create the MedSAM model²¹. The SAM model has three components, illustrated in Fig. 5b: an image encoder, a flexible prompt encoder, and a fast mask decoder. These components are described at a high level here.

3.2.1 Image Encoder

SAM utilizes a pre-trained Vision Transformer (ViT)²² that is adapted to process high-resolution inputs. This encoder runs once per image and can efficiently process the image before any prompting.

3.2.2 Prompt Encoder

In the original SAM model, two types of prompts are considered: sparse (points, boxes, text) and dense (masks). These prompts are transformed into an embedding and combined element-wise with the image embedding. To make the model fully automated it can be supplied with the bounding box of the full image and the model predicts masks for all available foreground objects.

3.2.3 Mask Decoder

The mask decoder takes the image embedding and the prompt embeddings to produce a mask. It employs a modified transformer decoder block which uses prompt self-attention and cross-attention to update all

embeddings²³. The output of these attention layers is upsampled, and a fully connected layer maps the output token to a dynamic linear classifier, which computes the mask foreground probability at each image location.

3.3 Loss

Segmentation models are typically trained using stochastic gradient descent which optimizes a loss function computed over the final layer. We used binary cross entropy as our loss function:

$$\mathcal{L}_{\text{bce}} = y \ln(p) + (1 - y) \ln(1 - p), \quad y \in \{0, 1\}. \quad (1)$$

4 Experiment and Result Analysis

In this section, we explain the details of the used datasets, along with the parameters for data preprocessing and model training. Additionally, we analyze the results produced from the experiments.

4.1 External Dataset

Alongside evaluating the trained models on the test partition of our dataset, we performed out-of-domain evaluation on a publicly available soft tissue sarcoma dataset (STS)¹², accessible via The Cancer Imaging Archive²⁴. This dataset consisted of 51 patients with sarcomas located in the extremities, sourced from various sites and scanners, resulting in high heterogeneity. Each patient’s data contained four different imaging modalities, including two paired MRI scans (T1 and T2) and a PET/CT scan. The MRI and PET/CT scans were conducted on different days, leading to variations in body positioning and anatomy. Tumor annotations are already provided in the dataset, delineated on the T2 scans. Additionally, we co-registered each T1 image onto the corresponding T2 image using the ANTs¹⁴ algorithm in 3D Slicer. However, while processing the dataset we found two image pairs with excessive movement between the modalities that were excluded in our analysis. The processed STS data in the 3D NIfTI format is publicly available at [provideurl](#).

4.2 Experimental Details

The 3D MRI images were resampled to have a voxel size of $1 \text{ mm} \times 1 \text{ mm} \times 1 \text{ mm}$. The intensity values of each image were clamped between 0.05% and 99.95% of the distribution of that particular image intensities to exclude outliers. The images were normalized using the min-max normalization procedure where the minimum and maximum intensities were image dependent. In the axial, sagittal, and coronal direction of the volume, 3 consecutive slices were grouped to create a 2.5D slice. Slices with more than 100 tumor voxels were used to train the model. We used 5-fold cross-validation over the 199 patients. The input size to the model was 256×256 . Padding or cropping was done if needed. The augmentations used were random crop, horizontal, vertical flip, gamma, brightness, contrast, Gaussian blur, motion blur, and grid distortion.

For the U-Net encoder, we used the pre-trained `se_resnext50_32x4d`²⁵ model and for the SAM image encoder we used the LiteMedSam model (a smaller version of the MedSAM model with a similar performance) weights which was provide in²¹. While training the segmentation models we fine tuned both the encoder and the decoder. The performance of the models was evaluated using Dice coefficient (Dice), i.e.,

$$\text{Dice} = \frac{2\text{TP}}{2\text{TP} + \text{FP} + \text{FN}} \quad (2)$$

Model	Input Modality	Train Domain	Test Domain	
			STS	MSTT-199
U-Net	MRI	MSTT-199	0.79	0.68
LiteMedSAM	MRI	MSTT-199	0.80	0.67
Multi-Branch U-Net ¹⁰	MRI, PET	STS	0.77	-

Table 2. Performance comparison of the segmentation models trained on the various datasets. The models trained on the MSTT-199 dataset outperform existing benchmarks.

. Here, TP is true positive, FP is false positive, FN is false negative. The full details of the training parameters are listed in Appendix A. During inference the images were resized to 256×256 . We did test time augmentations during the inference (horizontal and vertical flip, rotated by 90°) of each slice and the average output was taken. For each image volume, we conducted inference in the axial, coronal, and sagittal direction and averaged the output.

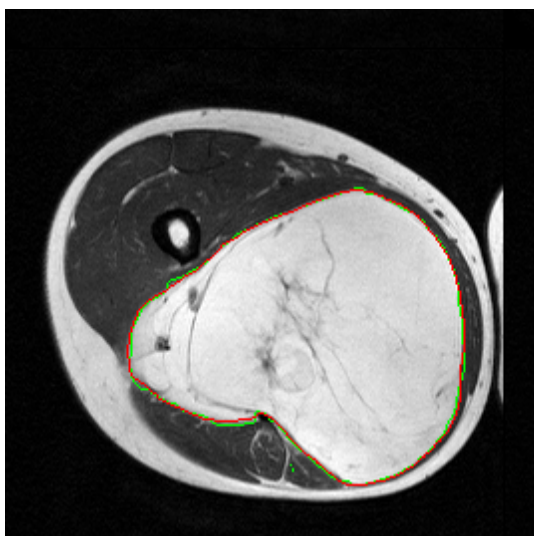
4.3 Result Analysis

Tissue Type	Dice
Fibrous	0.507
Fat	0.744
Myxoid	0.823
Nerve	0.748
Vascular	0.584
Average	0.681

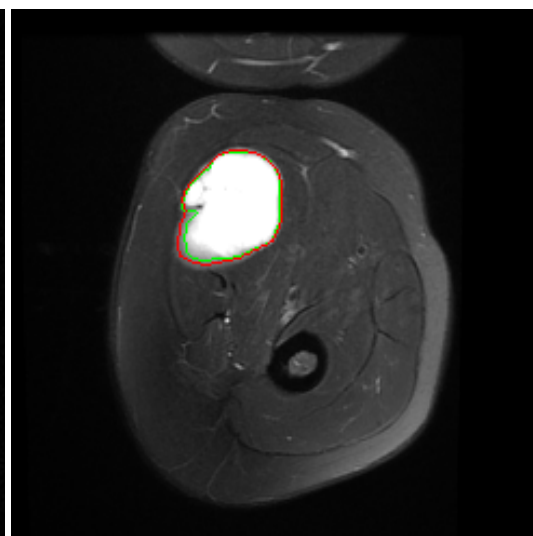
Table 3. Average dice score for different tumor tissue types.

In Table 2, we report the mean dice score achieved in the 5-fold cross-validation experiment in the MSTT-199 dataset as well as the STS dataset and compare it with the existing model in the literature. For the STS dataset, there is no predefined test set, so we evaluate our model on the whole dataset. The existing Multi-Branch U-Net¹⁰ model uses a 5-fold cross-validation approach (which involves domain-specific training). Additionally, it uses multiple imaging modalities (MRI and PET) as input. Whereas, our simpler U-Net with no domain-specific training, outperforms the existing benchmark. This shows the diversity and usefulness of our dataset. Lower Dice scores on the MSTT-199 test domain show that our dataset has much harder samples compared to STS. Additionally, we observe that the LiteMedSAM model does not outperform the U-Net-based model. This is probably because the LiteMedSAM did not have an STT segmentation dataset in its large-scale pretraining phase and may not have learned features that are related to the STT segmentation task. Additionally, it’s pretraining task was a semi-supervised prompting based approach where a tumor bounding box was provided alongside images. Without this additional information the model performance seems to suffer.

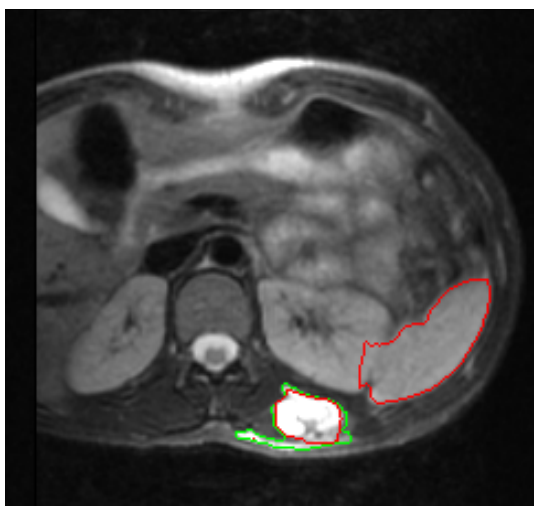
In Table 3, we report the average Dice score obtained across tissue types and show the distribution spread using boxplots in Fig. 7. The models perform best in segmenting myxoid and Fat tumors and perform worst in fibrous and vascular tissue types. Fat and myxoid tumors generally have a large homogeneous structure and are easy to differentiate from the background. Fibrous and vascular tissue



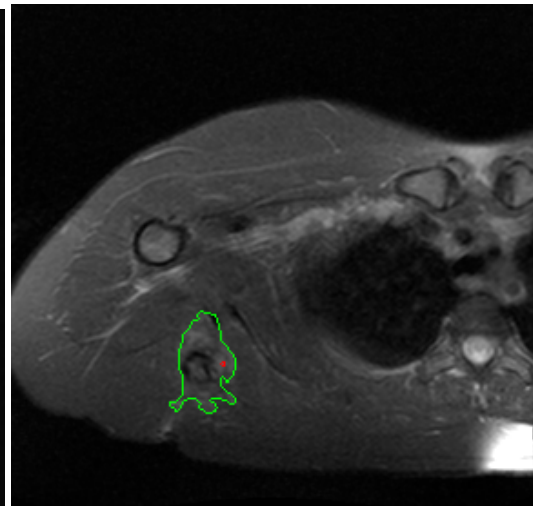
Large homogeneous Fat tumor in the thigh.



Medium sized homogeneous myxoid tumor in the thigh.



Small vascular tumor in the presence of confounding tissue structures in the flank (a less represented anatomy).



Small fibrous tissue structure not easily distinguishable from surrounding tissue in the chest wall (another less represented anatomy).

Figure 6. Examples of model predictions. The top row shows examples where the model successfully draws the contour around the image and the bottom rows show failures. The green contour denotes ground truth and the red contour denotes model predictions.

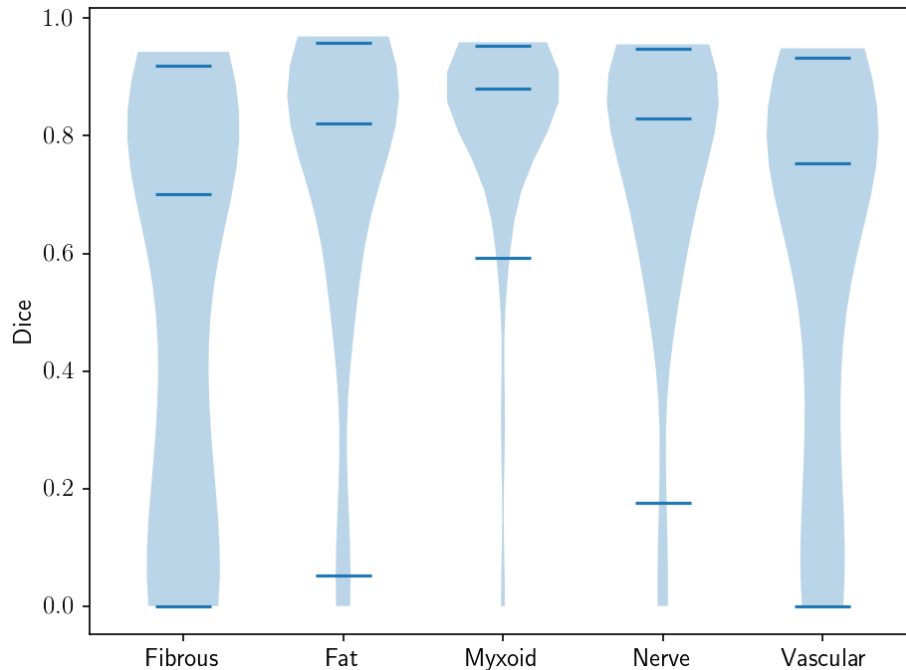


Figure 7. Dice distribution across tissue types.

often have a heterogeneous structure making it difficult to differentiate from the surrounding tissue. We visually confirm our observations in Fig. 6. A larger list of prediction failure montages can be found in Appendix B.

4.4 Effect of Volume

In general, larger tumor volumes are easier to segment for the model. Fig. 8 shows the performance variation of the model across different tissue types. Especially for the fibrous tissue type, there's a clear trend of performance increase with volume.

4.5 Effect of Anatomy

In Table 4, we report the average Dice scores across different tumor locations. As expected, the model does better in the extremities compared to the non-extremity locations due to having more sample representation in the training set.

4.6 Effect of Tumor Intensity

There is a weak positive correlation between average tumor intensity in the T1 image and dice scores for Fat tissue (Fig. 9). This is expected as lipid content is more distinguishable in the T1 image. However, for the rest of the tissue types, an increase in brightness has a no positive effect on tumor localization as those tissues are generally darker in the T1 image.

4.7 Suggestion on Future Data Collection

Although our dataset is large enough to train a state-of-the-art model, our result analysis suggests a dire need for a larger dataset to capture more diversity of tissue structures. Although we have set up a balanced dataset in terms of tissue types, there is an imbalance in terms of anatomy. In Table 1, we see fibrous and vascular tissue types have diverse anatomical representations. As observed in Table 3 and Table 4, these

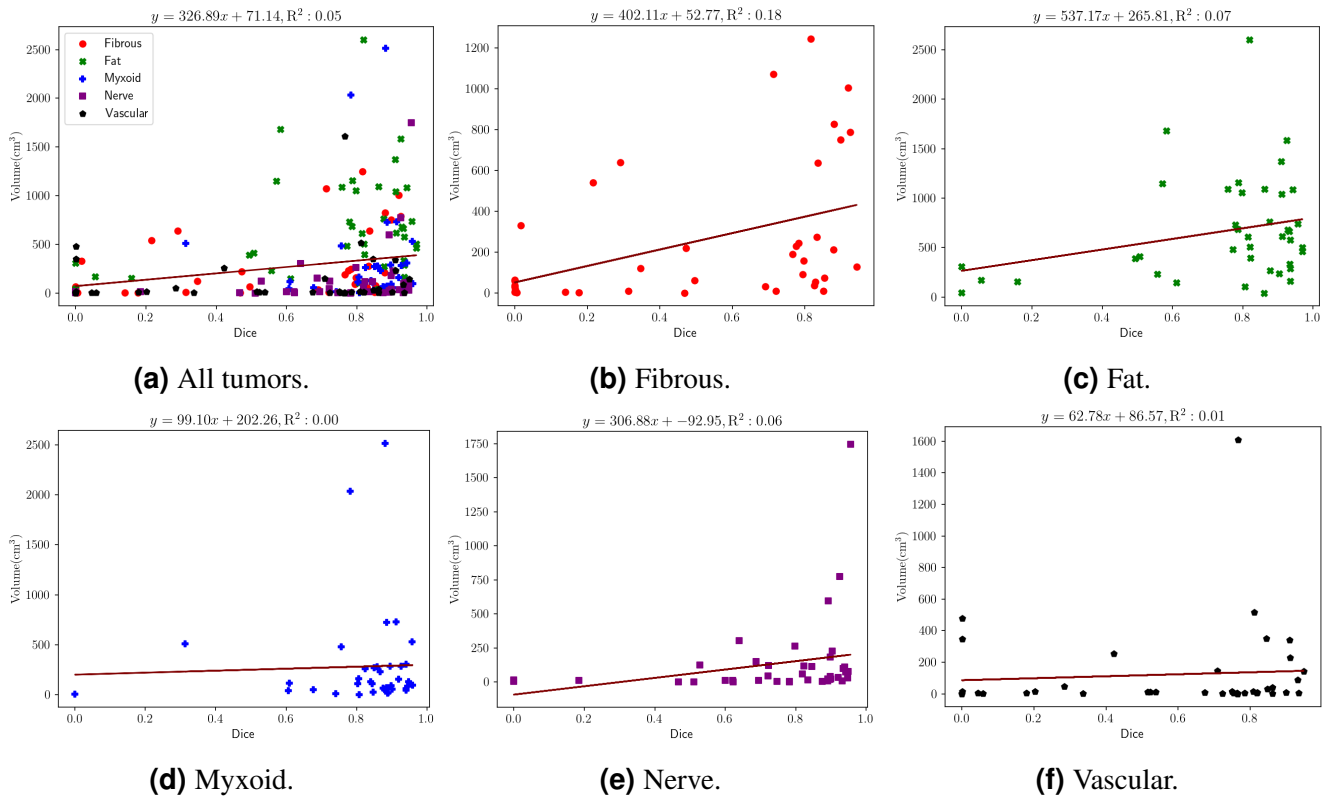


Figure 8. Effect of tumor volume on segmentation performance. The trend line equation and R^2 value is shown for the tissue types. It is difficult for the model to detect small fibrous tumors.

tissue types have poorer Dice scores compared to myxoid and Fat, even in the most common anatomical locations such as the extremities. The lesser representation of these difficult tissue types adds up with the challenging visual characteristics (small size, unclear tumor boundaries) and worsens the learning capability of the model. Future iterations of this dataset should focus on collecting more of these less representative and diverse tissue types.

5 Conclusion

In this work, we have described the creation of an MSTT dataset. We have trained a segmentation model on this dataset and benchmarked its performance on a publicly available dataset which achieves state-of-the-art result on MSTT segmentation. Results show that the segmentation models work well for the Fat, myxoid, and nerve tumors but struggle to segment tumors on fibrous and Vascular tumors. The segmentation model is sensitive to the volume of the tissue as well as the tumor location. Although this is the largest tumor segmentation dataset created, the size of the dataset needs to be increased further to make the segmentation models more robust. Special priority needs to be given to the tumors with fibrous and vascular tissue types as they have diverse anatomical locations and have challenging visual characteristics compared to Myxoid, Fat, and Nerve tissue.

References

1. Goldblum, J. R., Weiss, S. W. & Folpe, A. L. *Enzinger and Weiss's soft tissue tumors E-book* (Elsevier Health Sciences, 2013).

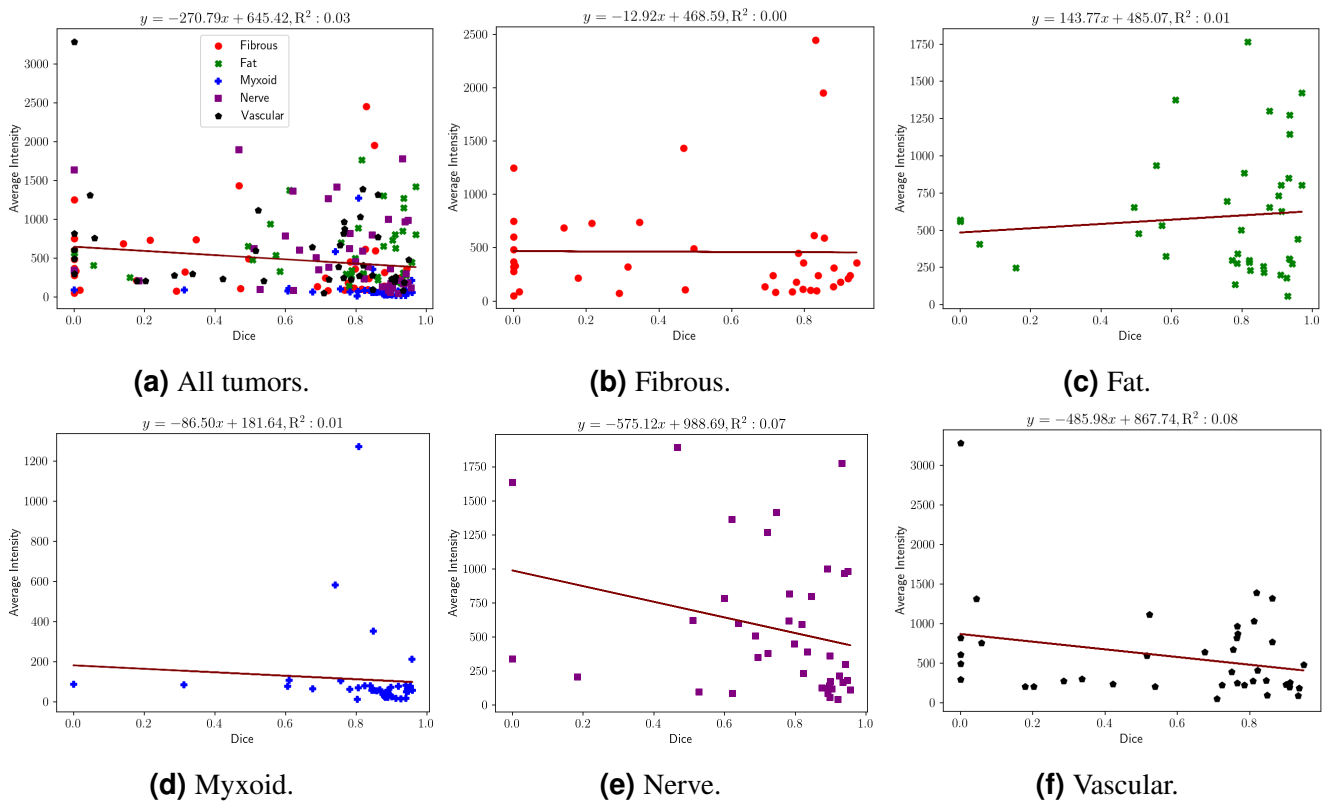


Figure 9. Effect of average tumor intensity (T1 image) on segmentation performance. For the fat tumors, there is a weak correlation of dice improvement with the increase of intensity.

Tumor Site	Tissue Type					Total Count	Avg. Dice
	Fibrous	Fat	Myxoid	Nerve	Vascular		
thigh	0.701	0.775	0.827	0.818	0.746	103	0.774
leg	0.223	0.893	0.740	0.612	0.301	25	0.505
glute	-	0.477	0.815	0.842	0.356	19	0.711
forearm	0.000	-	-	0.877	0.723	13	0.715
arm	0.738	0.895	-	0.540	-	10	0.596
hand	-	-	-	0.787	0.245	4	0.381
shoulder	0.474	-	-	-	0.493	4	0.485
foot	0.058	-	-	0.278	0.718	3	0.351
neck	0.284	-	-	-	0.663	3	0.411
pelvis	0.922	-	-	0.561	0.448	3	0.595
chest wall	0.173	-	0.898	-	-	3	0.415
abdomial wall	0.020	-	-	-	-	2	0.020
axilla	-	-	-	0.276	-	1	0.276
back	0.325	-	-	-	-	1	0.325
flank	-	-	-	-	0.148	1	0.148

Table 4. Average Dice score distribution for different anatomical locations. Missing values mean that the dataset did not contain a tumor of that type in that particular anatomical location.

- Cormier, J. N. & Pollock, R. E. Soft tissue sarcomas. *CA: a cancer journal for clinicians* **54**, 94–109 (2004).
- Lawrenz, J. M. *et al.* Can radiomics and machine learning predict diagnosis in musculoskeletal myxoid soft tissue tumors? *J. Am. Coll. Surg.* **235**, S61–S62 (2022).
- Cui, C. *et al.* Multi-modality classification between myxofibrosarcoma and myxoma using radiomics and machine learning models. In *Medical Imaging 2022: Computer-Aided Diagnosis*, vol. 12033, 782–788 (SPIE, 2022).
- Fields, B. K. *et al.* Whole-tumor 3d volumetric mri-based radiomics approach for distinguishing between benign and malignant soft tissue tumors. *Eur. radiology* **31**, 8522–8535 (2021).
- Lee, S. *et al.* Ensemble learning-based radiomics with multi-sequence magnetic resonance imaging for benign and malignant soft tissue tumor differentiation. *Plos one* **18**, e0286417 (2023).
- Dionisio, F. C. F. *et al.* Manual versus semiautomatic segmentation of soft-tissue sarcomas on magnetic resonance imaging: evaluation of similarity and comparison of segmentation times. *Radiol. Brasileira* **54**, 155–164 (2021).
- Blackledge, M. D. *et al.* Supervised machine-learning enables segmentation and evaluation of heterogeneous post-treatment changes in multi-parametric mri of soft-tissue sarcoma. *Front. oncology* **9**, 941 (2019).
- Bi, L. *et al.* Hybrid cnn-transformer network for interactive learning of challenging musculoskeletal images. *Comput. Methods Programs Biomed.* **243**, 107875 (2024).

10. Neubauer, T. *et al.* Soft tissue sarcoma co-segmentation in combined mri and pet/ct data. In *Multimodal Learning for Clinical Decision Support and Clinical Image-Based Procedures: 10th International Workshop, ML-CDS 2020, and 9th International Workshop, CLIP 2020, Held in Conjunction with MICCAI 2020, Lima, Peru, October 4–8, 2020, Proceedings 9*, 97–105 (Springer, 2020).
11. Diao, Z., Jiang, H., Han, X.-H., Yao, Y.-D. & Shi, T. Efnct: evidence fusion network for tumor segmentation from pet-ct volumes. *Phys. Medicine & Biol.* **66**, 205005 (2021).
12. Vallières, M., Freeman, C. R., Skamene, S. R. & El Naqa, I. A radiomics model from joint fdg-pet and mri texture features for the prediction of lung metastases in soft-tissue sarcomas of the extremities. *Phys. Medicine & Biol.* **60**, 5471 (2015).
13. Tkachenko, M., Malyuk, M., Holmanyuk, A. & Liubimov, N. Label Studio: Data labeling software (2020–2022). Open source software available from <https://github.com/heartexlabs/label-studio>.
14. Avants, B. B. *et al.* A reproducible evaluation of ants similarity metric performance in brain image registration. *Neuroimage* **54**, 2033–2044 (2011).
15. Fedorov, A. *et al.* 3d slicer as an image computing platform for the quantitative imaging network. *Magn. resonance imaging* **30**, 1323–1341 (2012).
16. Tkachenko, M., Malyuk, M., Holmanyuk, A. & Liubimov, N. Label studio: Data labeling software. *Open source software available from <https://github.com/heartexlabs/label-studio>* **2022** (2020).
17. Morrison, B. A. Soft tissue sarcomas of the extremities. In *Baylor University Medical Center Proceedings*, vol. 16, 285–290 (Taylor & Francis, 2003).
18. Ronneberger, O., Fischer, P. & Brox, T. U-net: Convolutional networks for biomedical image segmentation. In *Medical Image Computing and Computer-Assisted Intervention–MICCAI 2015: 18th International Conference, Munich, Germany, October 5–9, 2015, Proceedings, Part III 18*, 234–241 (Springer, 2015).
19. Fukushima, K. Visual feature extraction by a multilayered network of analog threshold elements. *IEEE Transactions on Syst. Sci. Cybern.* **5**, 322–333 (1969).
20. Kirillov, A. *et al.* Segment anything. In *Proceedings of the IEEE/CVF International Conference on Computer Vision*, 4015–4026 (2023).
21. Ma, J. *et al.* Segment anything in medical images. *Nat. Commun.* **15**, 654 (2024).
22. Dosovitskiy, A. *et al.* An image is worth 16x16 words: Transformers for image recognition at scale. *arXiv preprint [arXiv:2010.11929](https://arxiv.org/abs/2010.11929)* (2020).
23. Vaswani, A. *et al.* Attention is all you need. *Adv. neural information processing systems* **30** (2017).
24. Clark, K. *et al.* The cancer imaging archive (tcia): maintaining and operating a public information repository. *J. digital imaging* **26**, 1045–1057 (2013).
25. Xie, S., Girshick, R., Dollár, P., Tu, Z. & He, K. Aggregated residual transformations for deep neural networks. In *Proceedings of the IEEE conference on computer vision and pattern recognition*, 1492–1500 (2017).

A Training Parameters

List of augmentations used from the `albumentation` package:

- `PadIfNeeded (p=0.5)`,

- `RandomCrop(p=0.5)`,
- `RandomRotate90(p=0.5)`,
- `VerticalFlip(p=0.5)`
- `HorizontalFlip(p=0.5)`,
- `RandomGamma(gammaLimit=(50, 200), p=0.5)`,
- `RandomBrightnessContrast(p=0.5)`,
- `GaussianBlur(p=0.5)`,
- `MotionBlur(p=0.5)`,
- `GridDistortion(numSteps=5, distortLimit=0.3, p=0.5)`,
- `Normalize(mean=0, std=1)`.

List of model parameters

- Learning rate: $1e-4$
- Batch size: 16
- Epochs: 5

B Prediction Failures

A list of images where the segmentation model has failed.

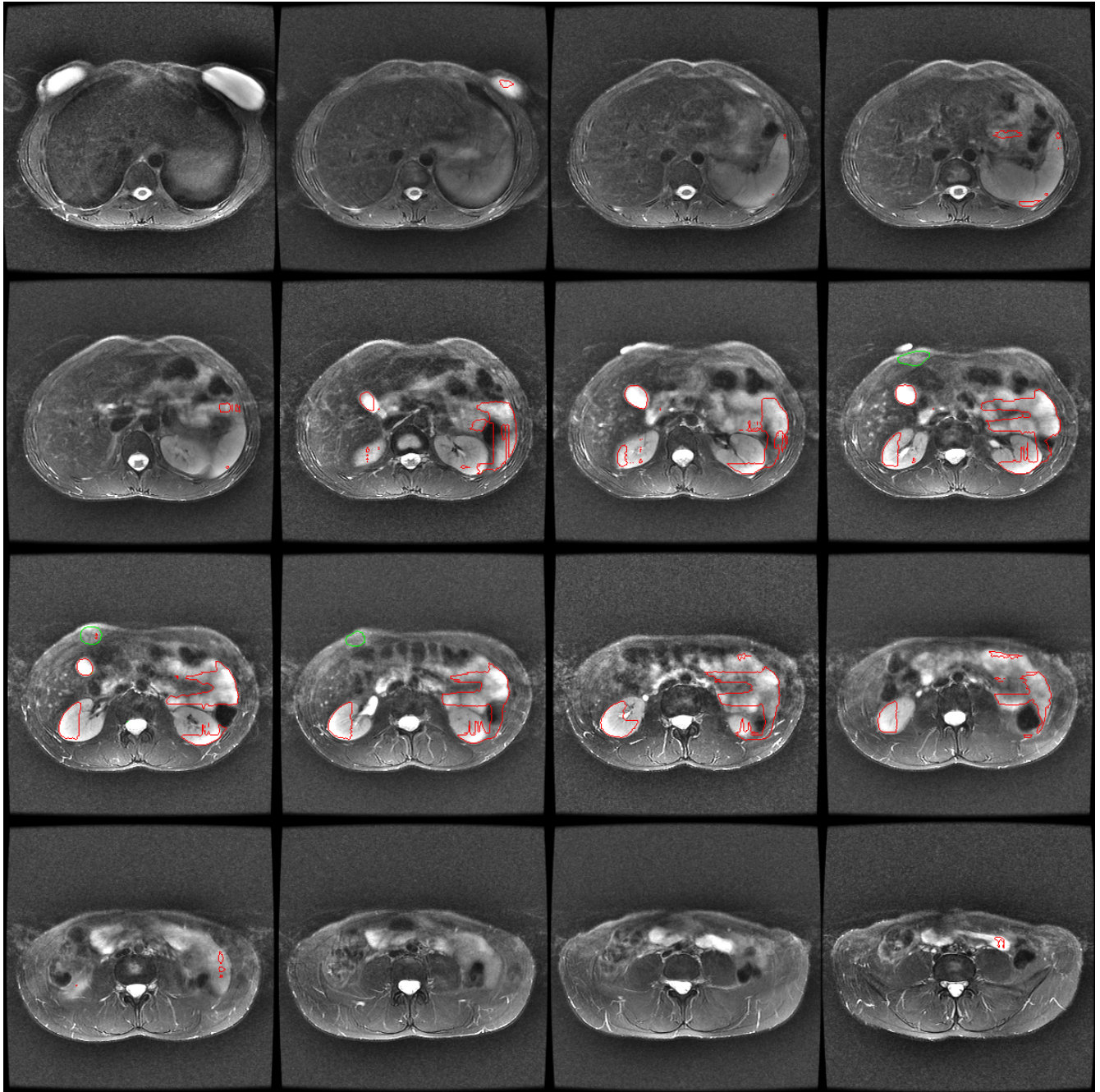


Figure 10. Fibrous tumor in the abdominal wall. There are confounding structures that create false positives. The tumor tissue gets mixed up with surrounding tissue creating weak boundaries. (Green contour is ground truth, red contour is prediction)

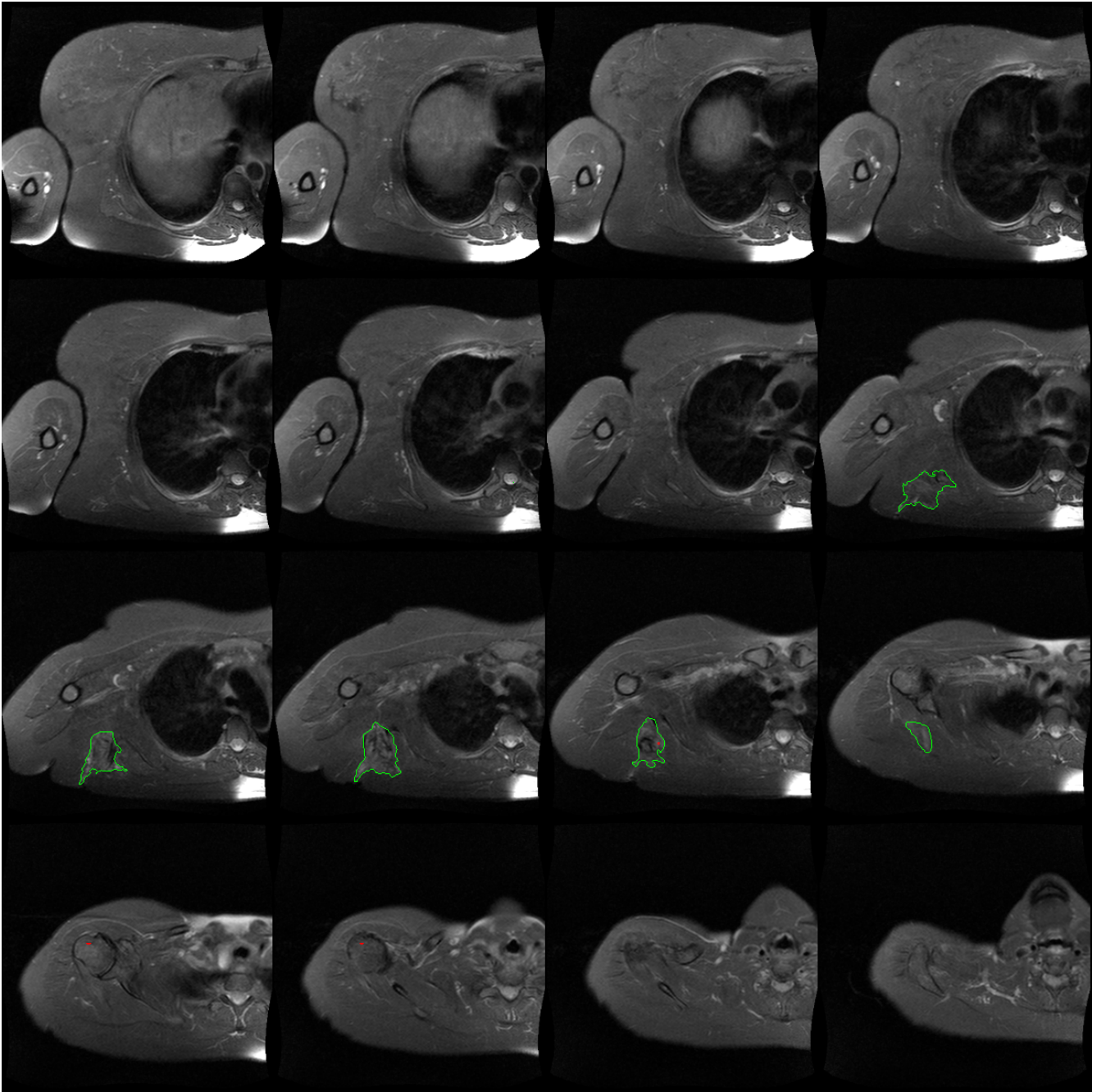


Figure 11. Fibrous tumor in the chest wall. The tumor tissue is not separable from surrounding tissue in terms of intensity and therefore has weak boundaries. (Green contour is ground truth, red contour is prediction)

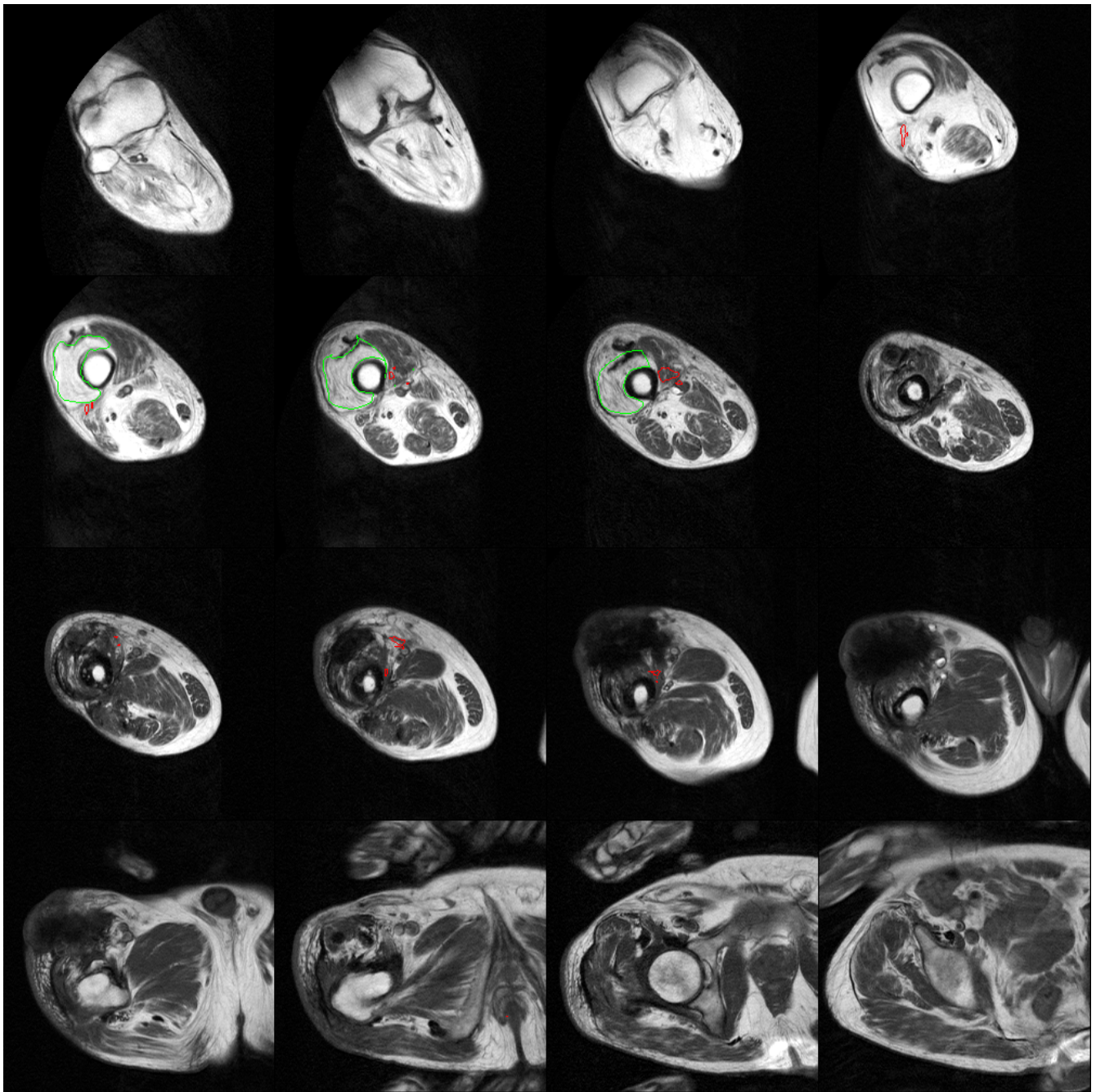


Figure 12. Fat tumor in the thigh. The tumor tissue is not separable from surrounding tissue in terms of intensity and therefore has weak boundaries. (Green contour is ground truth, red contour is prediction)

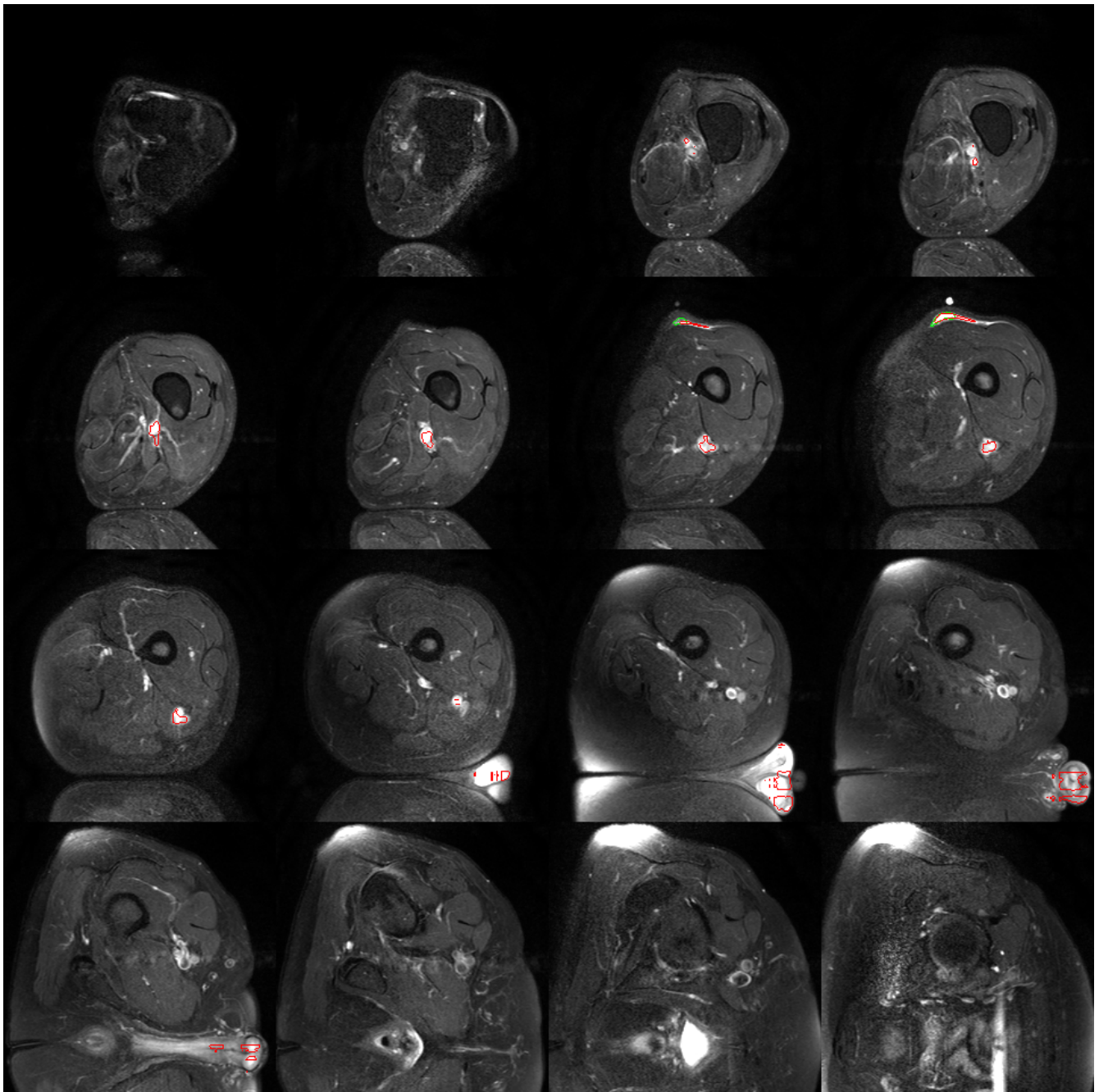


Figure 13. Myxoid tumor in the thigh. The testicles behave as confounding tissue creating false positives. (Green contour is ground truth, red contour is prediction)

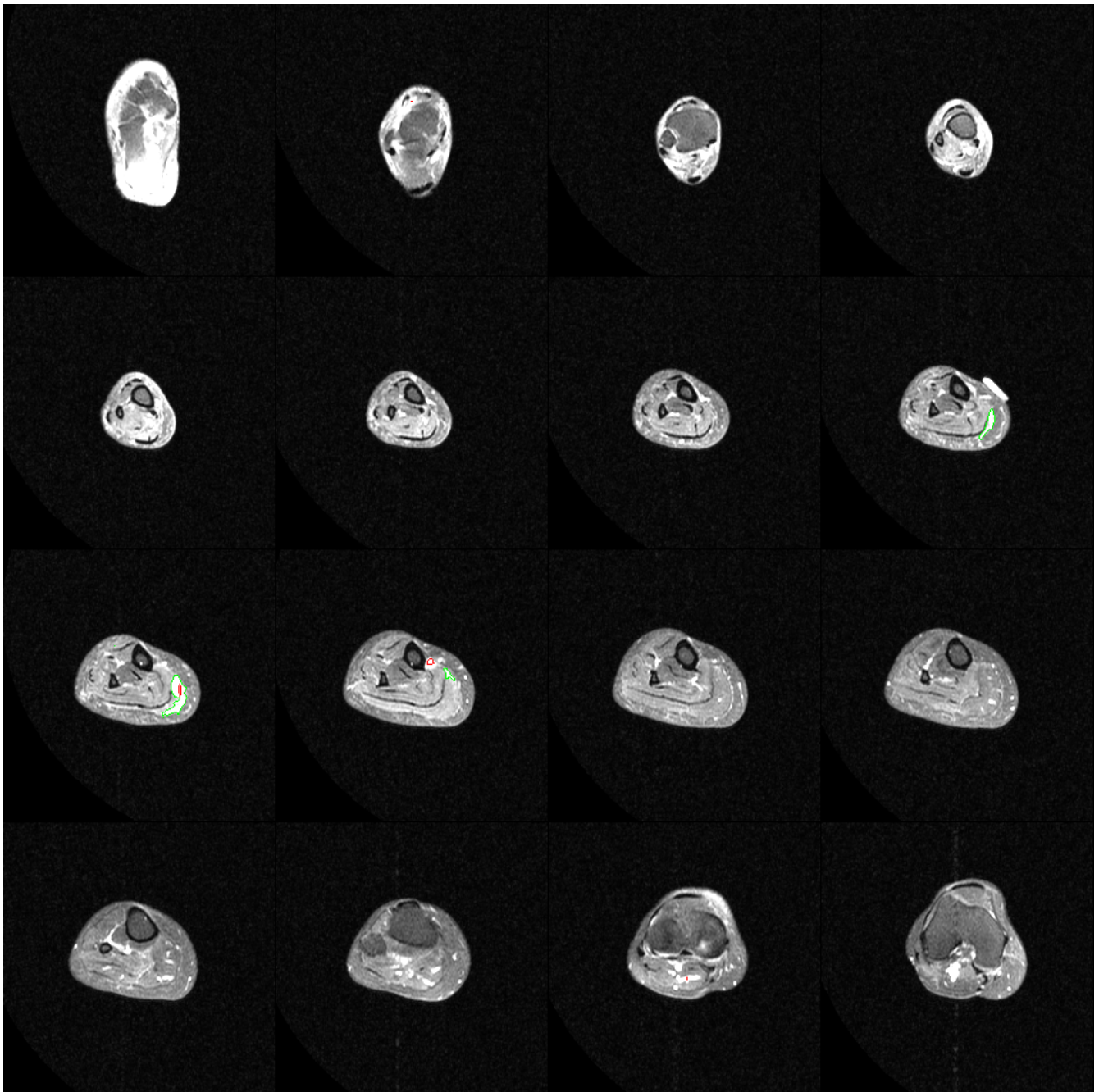


Figure 14. Nerve tumor in the leg. The tumor tissue is separable, but the image has artifacts confounding the model. (Green contour is ground truth, red contour is prediction)

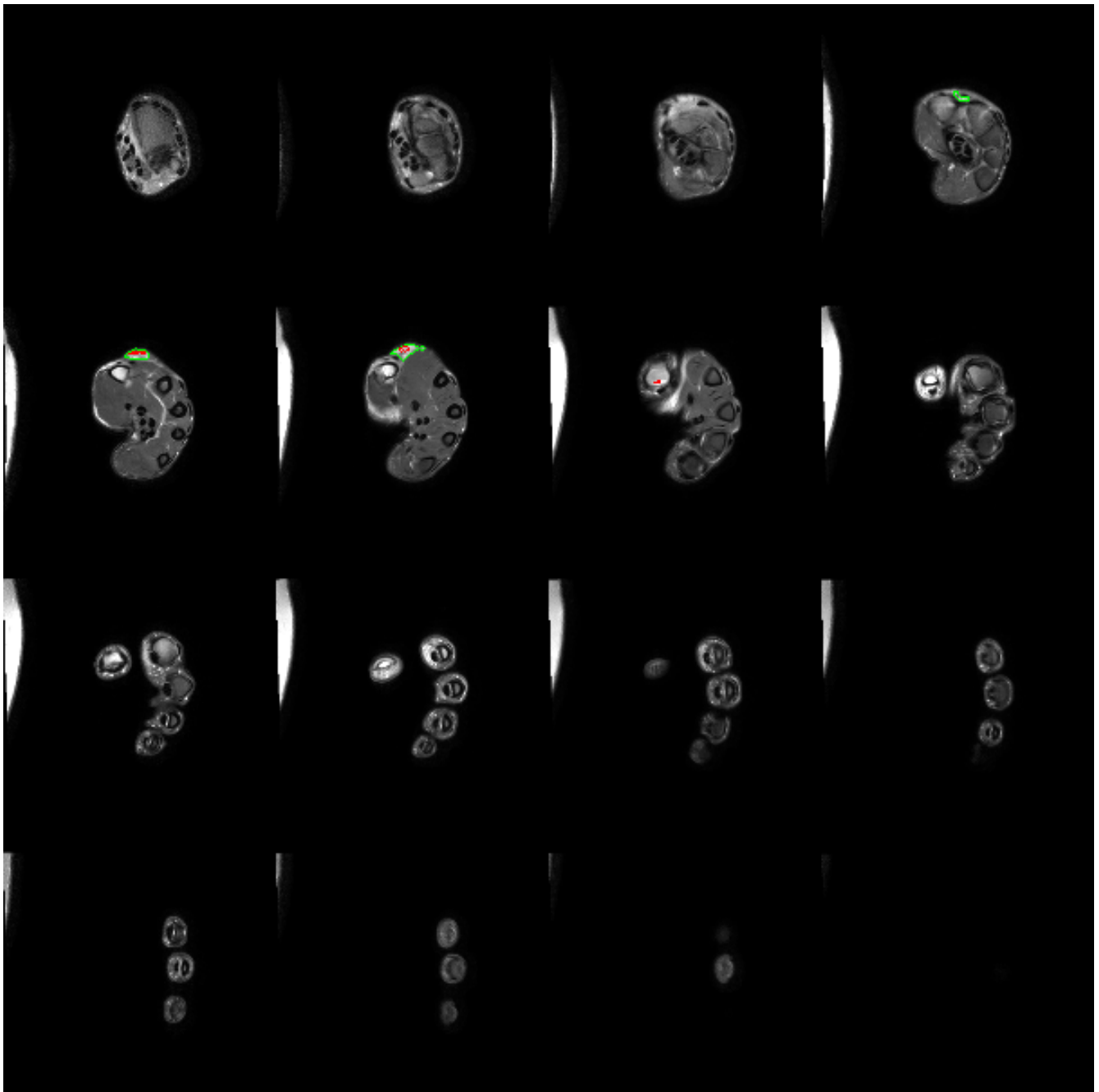


Figure 15. Vascular tumor in the hand. This is a rare anatomical structure with very few representations in the dataset. (Green contour is ground truth, red contour is prediction)

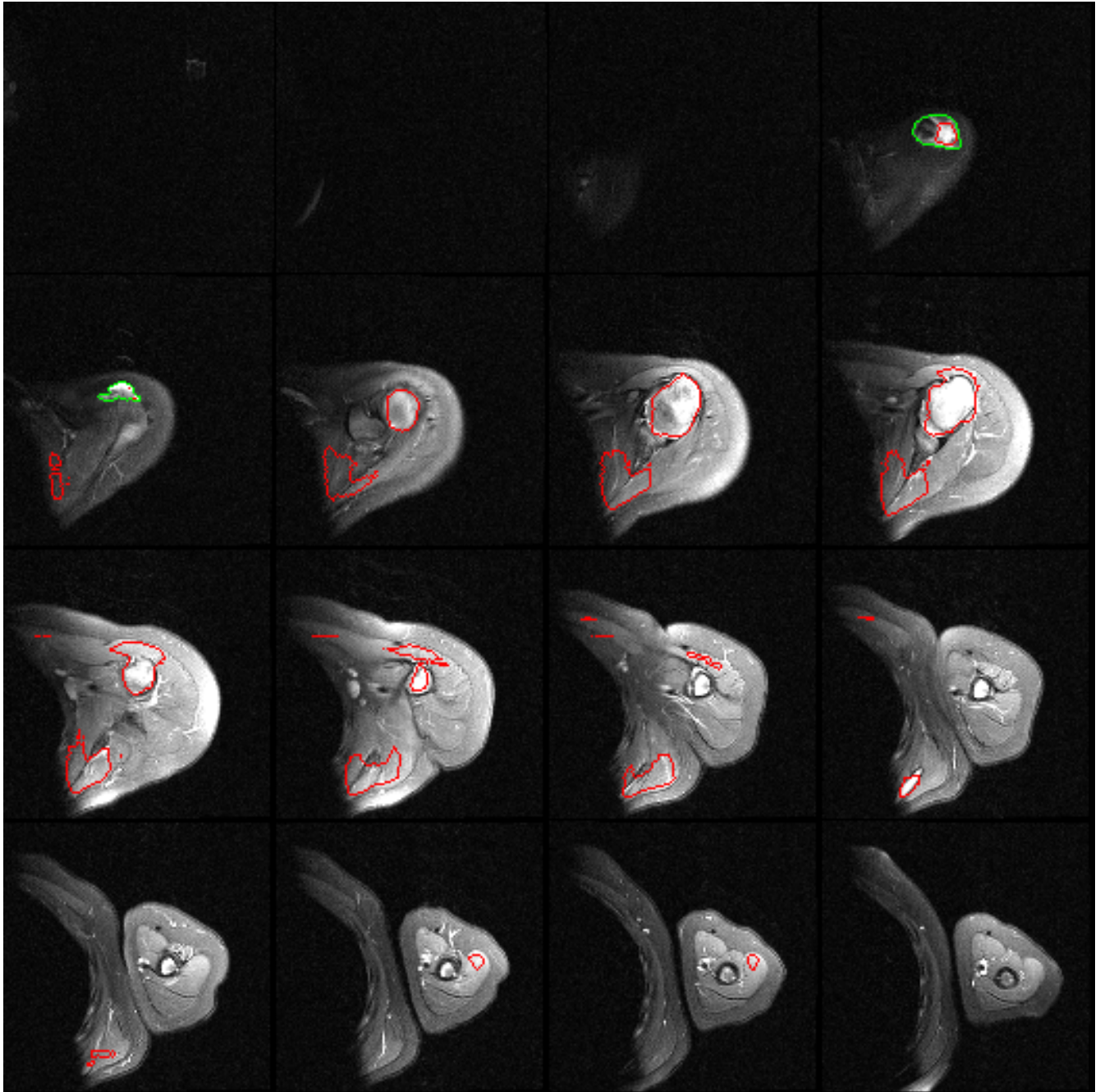


Figure 16. Vascular tumor in the shoulder. The tumor tissue has a heterogeneous structure, and the area with less intensity is not captured. Also, the bone confounds the model. (Green contour is ground truth, red contour is prediction)

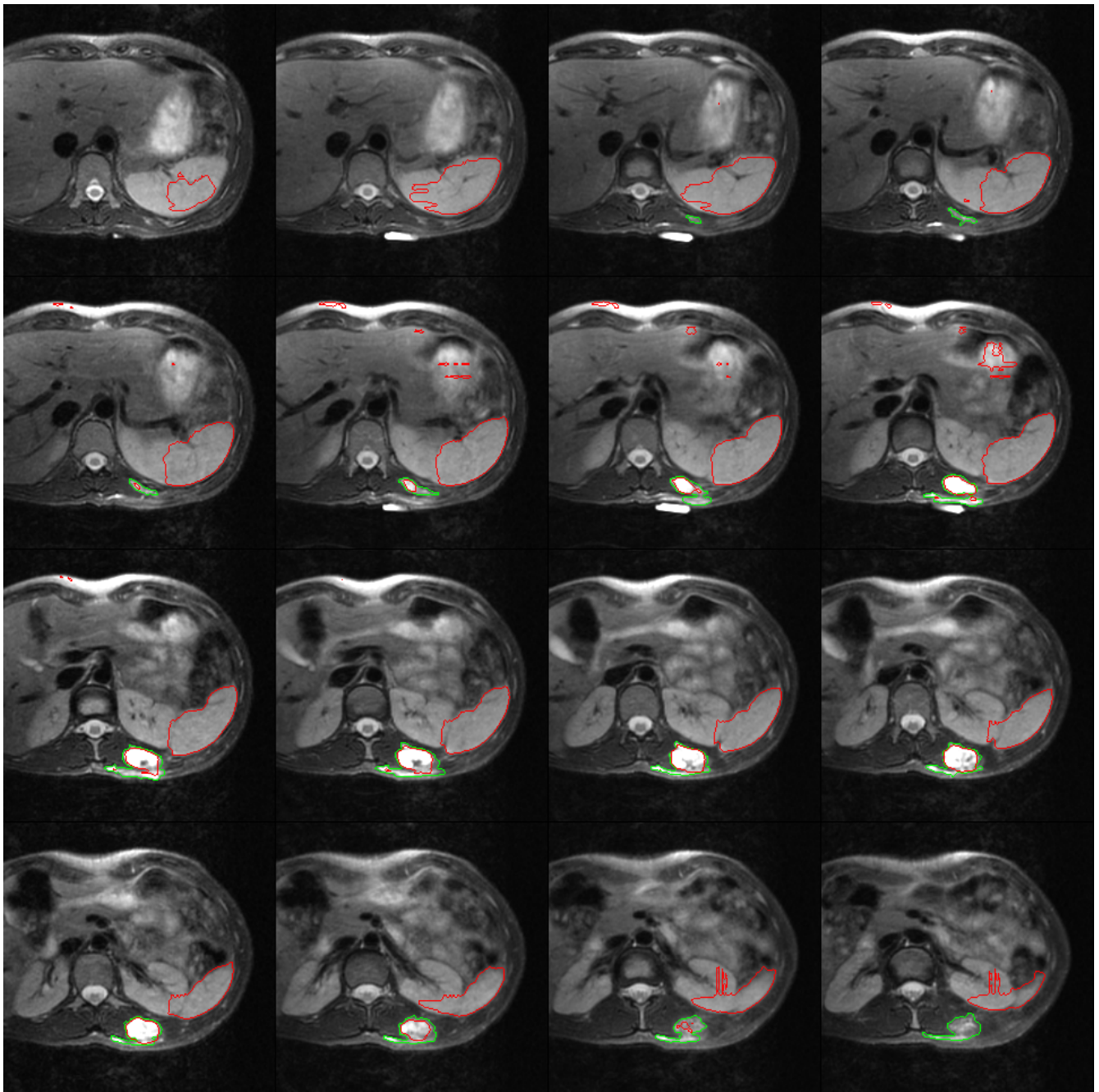


Figure 17. Vascular tumor in the flank. This is a rare anatomy, and the confounding structures create false positives. (Green contour is ground truth, red contour is prediction)